Controls on structural styles and decoupling in stratigraphic sequences with double décollements during thin-skinned contractional tectonics: insights from numerical modelling

Qingfeng Meng*[1], David Hodgetts

School of Earth and Environmental Sciences, University of Manchester, M13 9PL, UK

Abstract

Six series of particle-based numerical experiments were performed to simulate thin-skinned contractional tectonics in stratigraphic sequences with double décollements during horizontal shortening. The models were assigned with varying rock competence, depth and thickness of the upper décollement, which resulted in significantly different styles of deformation and decoupling characteristics above and below the upper décollement. The models composed of the least competent material produced distributed sinusoidal detachment folds, with many shallow structures profoundly decoupled from the deep-seated folds. The models composed of a more competent material are dominated by faulted, diapir-cored box folds, with minor disharmonic folds developed in their limbs. Differently, the results of models composed of the most competent material are characterised by localised piggyback thrusts, fault-bend folds and pop-up structures with tensile fractures developed in fold hinges. Depth of the upper décollements also plays an important role in controlling structural decoupling, i.e. the shallower the upper décollements, the higher the degree of decoupling becomes. Thicker upper décollements can provide sufficient mobile materials to fill fold cores, and contribute to the formation of secondary disharmonic folds, helping enhance structural decoupling. Our modelling results are comparable to the structural

[1] *Corresponding author. E-mail address: meng.qingfeng@hotmail.com

features exhibited in the Dezful Embayment of the Zagros Fold-and-Thrust Belt with the Miocene Gachsaran Formation acting as the shallow upper décollement, and the Fars with the Triassic Dashtak Formation as its intermediate décollement. This study demonstrates that rock competence, depth and thickness of the upper décollements can jointly affect the structural styles and decoupling, and are instructive for structural interpretation of deep zones in fold-and-thrust belts that exhibit distinct structural decoupling features.

Key words

structural decoupling; fold-and-thrust belt; décollement; discrete element; Zagros

1. Introduction

Thin-skinned deformation styles are typical of many fold-and-thrust (FAT) belts in the foreland of a collisional zone (Chapple, 1978). In such systems, a basal weak layer (e.g. shale and evaporite) serves as the main décollement that allows the deformed overburden to be detached on during shortening (Davis and Engelder, 1985). Two or multiple décollements have been reported in many FAT belts worldwide, such as the Apennines in Italy (Massoli et al., 2006), the Jura in Switzerland (Schori et al., 2015), the Subandean in Bolivia (Driehaus et al., 2014), the Kuqa in China (Izquierdo-Llavall et al., 2018), and the Zagros in Iran (Sepehr et al., 2006), among others. The occurrence of multidécollements can shape the variable geometry of FAT belts and affect forward propagation of deformation (Sherkati et al., 2006). In particular, the deformation above and below the upper décollement are commonly decoupled, which significantly increases structural complexity of the systems and makes it difficult to unravel deep structures beneath the upper décollement (Derikvand et al., 2018).

A thorough understanding of the styles of deformation and decoupling of FAT belts is crucial partially due to their economic importance, given the fact that FAT belts constitute the most prolific hydrocarbon provinces globally (Cooper, 2007). More fundamentally, this can yield insights into the competing mechanisms for accommodation of thin-skinned shortening (Erickson, 1996), i.e. thrusting, folding and diapirism (Bonini, 2003), and geologic conditions required for coupling/decoupling of deformation. Extensive field and seismic based observational studies (e.g. Motamedi et al., 2012; Najafi et al., 2018), analogue modelling (e.g. Borderie et al., 2018; Farzipour-Saein and Koyi, 2016) and numerical modelling studies (e.g. Ruh et al., 2012; Feng et al., 2015) have been conducted to address questions in FAT belts with double or multiple décollements. It has been realized that rock mechanical properties (Dean et al., 2013; Morgan, 2015; Meng and Hodgetts, 2019), décollements depth (Sepehr et al., 2006; Sherkati et al., 2006; Motamedi et al., 2012) and thickness (Stewart, 1996, 1999; Meng and Hodgetts, 2019) can determine the structural styles and decoupling in the shallow and deep segments of FAT belts. Nevertheless, a more comprehensive study of the combined impact of these parameters is needed.

This study reports a numerical modelling study of thin-skinned tectonics in FAT belts, with varying rock mechanical competence, thickness and depth of the upper décollement. The aims are 1) to produce realistic geologic structures comparable to natural examples; 2) to examine the controls on structural styles and the competing mechanisms for shortening accommodation in FAT belts with two dominant décollement levels; to 3) to investigate the role of the upper décollement in structural decoupling above and below the upper décollement. Notably, some other factors, such as existence of pre-existing structures (Callot et al., 2012), mechanical stratigraphy (Sepehr et al., 2006), basal décollement thickness (Meng and Hodgetts, 2019), synkinematic sedimentation

(Driehaus et al., 2014) and crustal shortening rate (McQuarrie, 2004), can also play an important role in structural development of a thin-skinned FAT belts with two or multiple décollements; however, this is beyond the scope of the current study. The modelling results presented here exhibit first-order structural similarities to the Fars and Dezful Embayment of the Zagros FAT Belt, and are believed to be of important implications for structural interpretation of deep zones in FAT belts with double or multiple décollements and prominent structural decoupling characteristics.

2. Methodology

2.1. Fundamentals of the discrete element method

The discrete element method is a particle-scale numerical method for modelling the bulk mechanical behavior of a system comprised of an assembly of discrete particles (Cundall and Strack, 1979). A single particle is treated as a rigid circular body that occupies a finite amount of space. A discrete element model is composed of distinct particles that displace independently from others, and elastically interact with their neighbouring particles at particle contacts using a soft touch approach. The particle contact is defined as a linear spring in compression (Fig. 1) that resists particle overlap, with the magnitude of particle overlap determined by the contact force via the force-displacement law. The particles are allowed to be bonded together by applying interparticle bonding at their contacts in order to resist both shear and extensional displacement. If either the normal or shear bond strength is exceeded, the bond breaks, indicating the formation of microfractures. Coalescence of adjacent microfractures leads to fracture propagation and formation of macro scale fractures. Slip between particles that is resisted by a frictional strength can occur between particles with unbonded contacts. The mechanical behaviour of a discrete element system is characterised by movement of each particle and inter-particle forces acting at particle contacts, which is governed by Newton's laws of motion. At all times, the forces acting on any particle are exclusively determined by its interaction with the particles with which it is in contact. The interaction of particles is regarded as a non-linear dynamic process with the states of equilibrium developing whenever the internal forces balance.

The discrete element method was initially developed to investigate the mechanical behavior of a granular media, which has been applied to soil and rock mechanics studies (Cundall and Strack, 1979). In recent year, the discrete element method has been effectively used for addressing questions in structural geology and tectonics. In particular, this method has been successfully adopted to simulate detachment fold (Hardy and Finch, 2005), fold-related fold (Benesh et al., 2007; Finch et al., 2003; Hardy and Finch, 2006; Hughes et al., 2014) and fold-and-thrust belt (Burbidge and Braun, 2002; Dean et al., 2013; Meng and Hodgetts, 2019; Morgan, 2015; Naylor et al., 2005), and is thereby considered to be an ideal method for the current study.

2.2. Model initial and boundary conditions

The Particle Flow Code (Cundall and Strack, 1999) software was employed to construct six series of two-dimensional discrete element models. Each model consists of a 20 km long, rectangular-shaped box filled with densely-packed circular particles (Fig. 1). All the models have a 150 m thick basal décollement that comprises 12653 particles. Models 1-9 of series 1 have a thinner upper décollement with a thickness of 75 m. Models 10-18 of series 4-6 have an equally thick upper décollement to the basal décollement. The upper décollement in the models of series 1 and 4 have the relatively shallowest burial depth, followed by models of series 2 and 5. Models of series 3 and 6 have the relatively deepest upper décollement. The stratigraphic units also contain eight homogeneous layers that represent the bulk rock. Each layer is 150 m thick and contains 1580 particles. The colours assigned for the layers do not indicate mechanical contrasts, but are simply used for bedding correlations.

The particle radii range from 5.0 to 10.0 m for the décollement layer (e.g. shale or salt), and 10.0 to 32.0 m for the bulk rock, both following a Gaussian distribution of particle size so as to inhibit hexagonal close packing of particles. Particle density is 2100 kg/m^3 for the décollement and 2600 kg/m^3 for the bulk rock. Interparticle friction was prescribed to be 0.4 throughout the bonded domain, and 0 within the décollements to ensure its low strength (Morgan, 2015).

The particle stiffness (normal and shear) of the bulk rock was set to be 1 x 10^7 N/m, which has been effectively used to represent sedimentary rocks (Liu and Konietzky, 2018). A bonding cohesion of 1.0, 2.5 and 5.0 MPa was prescribed to the three types of materials 1, 2 and 3. We then performed numerical rock mechanics tests following the procedure described by Cundall and Strack (1999), in order to derive the corresponding macroscopic mechanical parameters. In such tests, synthetic rock samples were created and loaded in a strain-controlled fashion by displacing the boundary walls at a sufficiently slow rate, so as to attain a quasistatic solution. The stresses and strains experienced by the rock sample were determined in a macro-fashion by summing the forces acting upon walls and tracking the relative distance between the walls. The test results reveal that the Young's Modulus for the three types of materials is 21.14 MPa, whilst the unconfined compressive strength (UCS) for materials 1, 2 and 3 is 1.87, 3.51 and 3.54 MPa, respectively.

The particles were packed by allowing randomly-generated particles to settle to the bottom of model under gravitational force. The system was considered to have reached static equilibrium when the mean unbalanced forces have been reduced to a negligible value. The particle assembly was then trimmed to the desired thickness, which gave rise to a small amount of vertical elastic rebound and surface uplift. This was followed by repeated trimming processes that allowed the system to be settled (Benesh et al., 2007).

The three elastic walls served as the confined boundaries for the particle assembly, and the upper surface was free. The left wall advanced at a controlled, uniform rate to the right, i.e. towards the foreland direction, to yield horizontal shortening and tectonic deformation in the system (Fig. 1). The models were gravitationally loaded by 1 g.

3. Results

3.1. Series 1

3.1.1. Model 1

The modelling result of model 1 is characterised by successive formation of multiple short-wavelength detachment folds that spread across the entire section (Fig. 2a). The first-order folds individually consist of multiple second-order parasitic folds that exhibit a much smaller fold wavelength and amplitude. The early-formed, symmetrical fold F1 is composed of two minor disharmonic folds in the inner units that have a vergence toward the hinge zone, and grew by consistent fold tightening with an increasing fold amplitude. F2 started to appear as a symmetric detachment fold since T4, and continued to grow till T7. At T6, a forethrust began to be initiated when the fold was right-verging, which was accompanied with a diapir rising from the basal décollement. During T6 to T7, F2 evolved into a fault-propagation fold as a result of propagation of the forethrust and a clock-wise rotation of its forelimb. Notably, the stratigraphic units above and below the upper décollement exhibit a profound structural decoupling, which is represented by the fact that the deep-seated folds barely propagated to the surface, and the superficial layer remained largely planar.

The model accommodated crustal shortening mainly by thickening across the entire system (Table 1). The variances in crustal thickening result in a rather smooth downslope with a slope angle of 9.3°. The diapirs in model 1 are much shorter than those in other models in this series.

3.1.2. Model 2

The deformation structures formed in model 2 are characterised by three similar-sized box folds, and five distinct diapirs originated from the basal decollement (Fig. 2b). Fold F1 was initiated as a symmetrical box fold with oppositely dipping axial surfaces and a sub-vertical diapir as its core. This was followed by the development of a minor fold F2 on the left of F1. Both folds continued to grow until T4 when F3 and F4 were initiated. During this period, the fold axes of F1 exhibited a slight clockwise rotation. F3 and F4 exhibited a right vengeance during T4 to T6, which constituted the inner disharmonic units of a larger fold. F5 began to develop at T6, and evolved into a regularly-shaped box fold.

Structural decoupling commonly occurred, which is represented by the development of minor disharmonic folds localised in the layers above the upper décollement. Such folds were developed in the limbs of the deeply rooted folds as secondary structures, and significantly affect the surface topography. The folds all propagated vertically to the surface, resulting in folding of the superficial layers above the upper décollement. The diapirs exhibit a more distinct geometry and a larger size than those in model 1 (Table 1). The accommodation of shortening was jointly achieved by vertical fold growth and diapirism.

3.1.3. Model 3

The modelling result of model 3 is characterised by the formation of piggy-back thrusts (Fig. 2c). Initially, F1 with disharmonic inner units were formed, which later developed into a fault-propagation fold with a forethrust, and subsequently into a fault-bend fold. The hangingwall layers were bent upward and transported passively along the ramp. F2 was formed at T4 and evolved into a fault-propagation fold with a forethrust at T5. As shortening continued, the hangingwall layers of the fault within F1 reached the backlimb of F2, resulting in a piggy-back arrangement of layers. At T6, the dispir inside F2 rose up to the level of the upper décollement, and subsequently propagated along the upper décollement. The persistent accumulation of displacement of the fault within F2 led to the formation of a minor pop-up structure located in the front of F2.

Structural decoupling occurred at T4, when a fault-propagation fold with a backthrust was formed in the superficial layers on the forelimb of F2. The pop-up structure formed in front of F2 caused significant uplift and buckling of the superficial rocks. The result of model 3 exhibits a strong strain localisation rather than distributed strain as shown in models 1 and 2. Horizontal shortening was mainly accommodated by the development of forethrusts, whilst the foreland remained largely undeformed (Table 1). This resulted in a dramatic uplift of the layers on the left of the model, and a relatively steep downslope of 39.1°.

3.2. Series 2

3.2.1. Model 4

The deformation of model 4 is characterised by successive formation of multiple sinusoidal minor detachment folds towards the foreland direction (Fig. 3a). Some folds contain second-order parasitic folds developed in their limbs. The folds developed above and below the upper décollement are approximately parallel, although significant differences appear locally.

The entire system has contributed to the accommodation of crustal shortening through thickening (Table 1). This produced a gentle downslope with a slope angle of 8.3°. Compared to the other two models in this series, model 4 exhibits the strongest structural decoupling.

3.2.2. Model 5

Model 5 successively produced three dominant asymmetric folds towards the foreland direction (Fig. 3b). F1 was initiated at T2 as a detachment, diapir-cored fold and subsequently evolved into a fault-propagation fold with a backthrust. The fold continued to grow from T2 to T5, which was accompanied with the growth of its dispir. A forethrust was generated in its forelimb at T4. At T5, a symmetric box fold F2 was initiated, which later became asymmetric by clockwise rotation of its forelimb. F3 was formed at T6, and evolved into fault-propagation fold with a backthrust. In this model, horizontal shortening was predominantly accommodated by folding and coeval diapirism. The undeformed foreland is 2.33 km long (Table 1).

3.2.3. Model 6

Model 6 produced two imbricate thrusts with the hangingwall layers of the early-formed thrust arranged as the first horse (Fig. 3c). F1 was initially formed at T3 as a diapir-cored, fault-propagation fold with a forethrust, which later evolved into a fault-bend fold. The diapir reached the surface at T4, and subsequently propagated in the sub-horizontal direction. F2 was formed on the right of the model as a fault-bend fold with a backthrust at T6. The system accommodated shortening mainly though fold vertical growth at the initial stage and accumulation of fault displacement at the later stage. Deformation is largely localised to the piggyback thrusts, and the unreformed foreland area reaches 5.26 km long (Table 1).

3.3. Series 3

3.3.1. Model 7

The modelling result of model 7 is characterised by successive formation of multiple short-wavelength sinusoidal folds below the upper décollement and larger folds above the upper décollement (Fig. 4a). The fold traces below and above the upper décollement are generally parallel, although disharmonic folds below the upper décollement occur locally. However, the amplitude and wavelength of the upper folds are much higher than the lower folds. The system accommodated crustal shortening mainly by thickening (Table 1). The variances in crustal thickening result in a downslope with a slope angle of 9.1°.

3.3.2. Model 8

Model 8 produced two dominant box folds and four diapirs during the shortening process (Fig. 4b). F1 was initially formed at T2 as a symmetric diapir-cored box fold, which became asymmetric at T3 by anticlockwise rotation of the fold axial plane. Interestingly, the fold axial plane of F1 rotated clockwise with its diapir core dipping towards the hinterland direction. This was accompanied with the formation of F2, a minor fold developed in the forelimb of F1. The diapir within F2 was dipping oppositely to that within F1, i.e. towards the foreland. Meanwhile, F3 was formed in the foreland as a fault-propagation fold with a backthrust. Later on, F1 and F2 had a vergence towards the fold hinge. F4, a minor fault-propagation fold with a forethrust, was formed in the forelimb of F3. Finally, F2 became merged with F1, and F4 merged with F3. Notably, F3 experienced a clockwise rotation of its axial plane. The system accommodated shortening mainly by growth of the two dominant folds. The undeformed foreland is 4.46 km long (Table 1).

3.3.3. Model 9

The modelling result of model 9 is characterised by the formation of a single dominant fault-bend fold in the foreland (Fig. 4c). Initially, the shortening was accommodated by uplifting and overturning of the layers on the left, followed by the down-going leftmost segment being sliced off the bulk rock during its clockwise rotation. At T4, F1 was initiated as a fault-propagation fold with a backthrust. A diapir intruded upwards along the thrust fault. Later on, the diapir penetrated through the upper décollement, accompanied with vertical growth of the fold and the hangingwall layers being passively transported along the ramp. Multiple reverse faults were formed in the forelimb of F1, i.e. hangingwall layers of the backthrust, during fold tightening. At T6, F1 passed into a fault-bend fold as it continued to accumulated displacement. A tensile fracture was formed in the fold hinge, and more reverse fractures were generated in the forelimb of F1. Following this, F1 accommodated shortening by incremental growth in the vertical direction. The tensile fracture in the fold hinge propagated downwards, with its aperture being enlarged.

Model 9 accommodated shortening mainly by vertical development of F1 and formation of secondary structures within F1. The height of the diapir as the core of F1 is the highest among all models (Table 1). The length of the unreformed foreland is longer than the other two models in this series.

3.4. Series 4

3.4.1. Model 10

Generally, the modelling result of model 10 is rather similar to that of model 1, which is characterised by successive formation of five dominant sinusoidal folds with numerous second-order parasitic folds developed in the limbs of larger folds (Fig. 5a). A strong decoupling occurs between the layers above and below the upper décollement. This is represented by the widespread folding in the lower units, whilst the superficial layers remained flat and smooth. Crustal thickening occurred throughout the system (Table 1), resulting in a downslope of 11.1° on the surface. Multiple minor diapirs rose up from the basal décollement, with a maximum height of 0.51 km (Table 1).

3.4.2. Model 11

The modelling result of model 11 is characterised by the formation of three dominant detachment fold and five diapirs (Fig. 5b). Initially, a minor fault-propagation fold with a forethrust was generated above the upper décollement. A minor diapir originated from the basal décollement rose up and led to the formation of F1 as an asymmetric box fold. Following this, a minor fault-propagation fold with a backthrust was developed in the forelimb of F1 above the upper décollement. Another diapir, close to the core of F1, was initiated ahead of F1 and caused gentle folding of the upper layers. Later on, F1 and F2 constituted a larger fold through vergence towards each other. At T4, two more folds F3 and F4 were formed as diapir-cored box folds. A fault-propagation fold with a backthrust was generated in the forelimb of F3 above the upper décollement. F3 and F4 merged into a larger fold at T6 that contains disharmonic inner units. Meanwhile, F5 was formed as a rather symmetric box fold, whose fold limbs were later cut by minor thrusts.

Model 11 accommodated shortening mainly through fold growth and diapirism. Notably, the system exhibits a strong structural decoupling, which is represented by (1) the disharmonic folds in the inner units of the first-order folds due to fold vergence; and (2) the secondary minor folds and thrusts developed in the limbs of the deep-seated folds. The disharmonic folds significantly increase the structural complexity of the system and the irregularity of the surface topography.

3.4.3. Model 12

The modelling result of model 12 is distinctively represented by the formation of piggyback thrusts that exhibit a strong deformation localisation (Fig. 5c). Initially, thrust faults were nucleated on the left of the model, with the hangingwall rocks being passively transported upwards along the ramp. This process was repeated for the second thrust developed ahead of the first thrust. At T3, F1 was formed as a fault-propagation fold that is associated with a hinterland-dipping diapir rising from the basal décollement. As shortening continued, the hangingwall layers of the early thrusts overrode the backlimb of F1, whilst the fold axes of F1 rotated clockwise. At T5, F1 evolved into a fault-bend fold, and the hangingwall layers of the thrust in F1 were transported along the thrust ramp towards the foreland direction. At the final stage, a fault-propagation fold F2 with a backthrust was formed ahead of F1. Disharmonic minor fault-propagation folds were generated in the limbs of F2. The accommodation of shortening was mainly achieved by the piggyback thrusts, aided by the later fault-propagation fold.

3.5. Series 5

3.5.1. Model 13

The modelling result of model 13 is comparable to that of model 4, which is characterised by successive formation of multiple sinusoidal detachment folds towards the foreland direction (Fig. 6a). The fold styles developed below and above the upper décollement exhibit variances, although the fold traces are locally parallel. Crustal thickening occurred throughout the system (Table 1). The variances in crustal thickening resulted in a downslope of the surface layer with a slope angle of 9.5°.

3.5.2. Model 14

Model 14 produced three dominant box folds and four diapirs (Fig. 6b). F1 was initiated during the rising up of a hingerland-dipping diapir from the basal décollement. This was accompanied with the development of a fault-propagation fold cutting the layers in the forelimb of F1 above the upper décollement. Later on, F1 experienced clockwise rotation of its forelimb and evolved into a fault-propagation fold with a forethrust. At T4, a secondary fold was formed in the backlimb of F1, with the development of a minor foreland-dipping diapir as its core. Following this, F2 was formed as a rather symmetric box fold in the foreland, whose axial planes rotated clockwise and caused F2 to become asymmetric at T6. F3 was then formed between F1 and F2 as a second order detachment fold, followed by the formation of F4 in the foreland area ahead of F2. A hinterland-dipping thrust fault was formed along the right axial trace of F4 in layers above the upper décollement. The system accommodated shortening by forth and back folding of the layers, coupled with development of thrusts within the folds. (Table 1).

3.5.3. Model 15

The modelling result of model 15 is characterised by in-sequence development of a fault-bend fold and a fault-propagation fold (Fig. 6c). Initially, a fault-bend fold was developed on the leftmost side of the model. The hangingwall fragment overrode the right layers, and became overturned as shortening continued, prior to the formation of F1 at T3. F1, which was initially formed as a fault-propagation fold with a forethrust, accumulated its reverse displacement and evolved into a fault-bend fold when the thrust reached the surface. Notably, a tensile fracture occurred in the central fold hinge and propagated downward. The diapir rooted in the basal décollement penetrated the upper décollement at T4, which led to the anticlinal breakthrough at T7. F2 was formed at T7 as a fault-propagation fold with a forethrust. A forethrust and backthrust developed in the backlimb of F2 cut the layers above the upper décollement, resulting in a minor pop-up structure. The system accommodated shortening mainly by fold development and also accumulation of reverse displacement of F1. The undeformed area in the foreland is 5.41 km long (Table 1).

3.6. Series 6

3.6.1. Model 16

Model 16 successively produced a series of sinusoidal detachment folds towards the foreland direction (Fig. 7a). The folds below the upper décollement exhibit a lower amplitude and wavelength than the upper folds. Disharmonic folds occurred in layers above the upper décollement as a result of vergence of neighbouring minor folds that constitute a larger fold. Other than the disharmonic folds, the fold traces below and above the upper décollement are largely parallel, and structural decoupling is less significant than that exhibited in model 10 and 13. Crustal thickening occurred throughout the system (Table 1), which results in a downslope angle of 13.1°.

3.6.2. Model 17

The modelling result of model 17 is characterised by the formation of four dominant box folds and seven diapirs (Fig. 7b). F1 was initially formed as a symmetric box fold with its core consisting of a sub-vertical diapir. The fold became tightened as shortening continued, resulting in thrust faults that propagated along both the fold axial traces. Later on, the axial plane of F1 had a clockwise rotation, resulting in the asymmetric geometry of F1. This was accompanied with the growth of its core diapir along the backthrust. Secondary folds were cut by reverse faults in the forelimb of F1. F2 was initiated at T3, which evolved to become a fault-propagation fold with a backthrust at T4. F2 then experienced tightening and a clockwise rotation with its core diapir steepened. During T4 and T5, two minor secondary folds F3 and F4 occurred on the left of F1 and F4, respectively. This was followed by the development of F5 at T6, and F6 at T7, both of which are fault-propagation fold with a forethrust. At T7 a minor diapir was initiated between F4 and F5, and caused gentle folding of the host layer, whilst the layers above the upper décollement were not influenced. Crustal shortening was mainly accommodated by in-sequence development of four dominant folds and back-and-forth formation of some minor diapirs.

3.6.3. Model 18

Model 18 produced a concave-up pop-up structure that consists of an early-formed fault-propagation fold with a backthrust, and a later fault-bend fold with a forethrust (Fig. 7c). The geometry of the pop-up structure is similar to that described by Alsop et al. (2017). F1 was initiated at T2 as a fault-propagation fold, and its fold axis subsequently experienced a clockwise rotation. Notably, its core diapir penetrated the upper décollement at T4, whilst the forelimb of F1 was cut by a thrust fault developed along the axial trace. At T5, F2 was formed with the diapir intruding upward along the forethrust. A backthrust was developed along fold axial trace when F2 became tightened as shortening continued. At T7, F2 evolved into a fault-bend fold as it accumulated reverse displacement, with a tensile fracture occurring in its hinge zone. Interestingly, F1 and F2 converged towards each other, which finally constituted a pop-up structure. The system accommodated shortening mainly by the pop-up structure, which is tightly associated with development of the two major thrusts. The undeformed area is 5.16 km long in the foreland (Table 1).

3.7. Summary of modelling results

3.7.1. Models with the same mechanical property

Models that are composed of the least competent material 1, exhibit similar structural styles, which are characterised by multiple short-wavelength, sinusoidal detachment folds (Fig. 8). The diapirs rooted in the basal décollement are much smaller than those in models composed of more competent materials. Shortening of the system resulted in crustal thickening across the entire section, resulting in a clear taper towards the foreland direction. Models that are composed of more competent material 2, all produced diapir-cored box folds. The diapirs in these folds are often inclined, resulting in an overall asymmetric fold geometry. The fold limbs are commonly faulted.

Models that are composed of the most competent material 3, are dominated by thrusts, fault-bend folds and pop-up structures. Strain localisation, represented by piggyback arrangement of forethrust and progressive accumulation of fault displacement during shortening, is distinct. Tensile fractures commonly occurred in fold hinge zones.

Structural decoupling between stratigraphic units above and below the upper décollement is the most profound in models composed of the least competent material 1, followed by those composed of more competent material 2. Models that are composed of the most competent material 3 exhibit the least features of structural decoupling.

3.7.2. Models with the same depth of the upper décollement

Models with the shallowest upper décollement exhibit the most significant structural decoupling above and below the upper décollement (Fig. 8). This is represented by the fact that the underlying, deep-rooted structures did not significantly affect the upper layers in models 1 and 10 with incompetent materials, and also represented by minor disharmonic folds and reverse faults developed above the upper décollement in other models. Pop-up structures that only occurred in the upper units also contributed to structural decoupling. Structural decoupling is much less common in models with a deeper upper décollement.

3.7.3. Models with the same thickness of the upper décollement

Generally, models (10-18) with equally thick décollements exhibit a more significant structural decoupling below and above the upper décollements (Fig. 8). Moreover, a thicker upper décollement tends to hinder vertical propagation of folds, and to promote lateral development of structures. This is evident by a larger number of folds and diapirs developed in models with an equally thick upper décollement to the basal décollement than models with a thinner upper décollement.

4. Discussion

4.1. Controls on structural styles

The final configuration of the thin-skinned fold belts produced in our models is represented by the formation of sinusoidal detachment folds, box folds, fault-propagation folds, fault-bend folds, pop-up structures, tensile fractures and piggyback thrusts (Fig. 8). Given the predefined boundary and initial conditions of the six series of models, it is possible to evaluate the geologic controls on the competing mechanisms of folding versus faulting versus diapirism that gave rise to the styles of deformation in the systems.

Each series of models, with the same boundary and initial conditions except bonding cohesion, exhibit significantly different structural styles, which can be represented by (1) models with the least competent material are dominated by short-wavelength, sinusoidal and disharmonic detachment folds; (2) models with a more competent material are dominated by faulted, diapir-cored box folds; and (3) models with the most competent material are dominated by thrusts, fault-bend folds and tensile fractures. This indicates that rock mechanical property plays a dominant role in controlling structural styles, agreeing with Morgan (2015) and Meng and Hodgetts (2019).

Depth of the upper décollement is tightly associated with the fold-dominated systems, where a deeper upper décollement favours a shorter wavelength of the folds developed below the décollement. Oppositely, a shallower upper décollement allows the deep-seated folds in the lower units to grow vertically and to attain a larger wavelength. For systems dominated by thrusts, structural styles are also significantly influenced by the depth of the upper décollement, i.e. a shallower upper décollement promotes transportation of hangingwall layers along the ramps of piggback forethrusts through accumulation of fault displacement, whilst a deeper upper décollement favours formation of backthrusts (Fig. 4c) or a combination of backthrusts and forethrusts (model 18) (Fig. 7c) to accommodate shortening.

The different modelling results of models with varied upper décollement thickness suggest that the thickness of the upper décollement is one of the factors that determined the structures produced within the systems. Such differences may be attributed to the fact that the upper décollement separates the upper units from the lower units and hindered vertical growth of folds by redistribution of weak décollement materials onto synclines. Moreover, a thicker upper décollement is more likely to cause the formation of minor structures in the upper units, e.g. fault-propagation folds and pop-up structures, especially in systems with a shallow upper décollement. This is possible because that flow of weak materials and the resulting thickness variation is more common in a thicker upper décollement during shortening, which can support fold development by material redistribution into fold cores as suggested by Stewart (1996).

4.2. Controls on structural decoupling

Our modelling results reveal that the models composed of the least competent material, exhibit the most significant structural decoupling above and below the upper décollement. This is represented by the fact that folds were formed disharmonically above the below the upper décollement (Fig.

8). Moreover, such materials promoted forward propagation of deformation and a more distributed strain rather than vertical growth of existing structures, which resulted in crustal thickening across the entire section (Table 1). The simple surface structures mask complex folds at depth. Conversely, models that are composed of more competent materials promoted vertical growth of structures and strain localisation. This favoured parallel folding in the upper and lower units, and hence contributed to structural coupling.

Another major control on structural decoupling is the depth of the upper décollement. The modelling results presented indicate that a shallow upper décollement favours the formation of minor parasitic structures in the limbs of deep-seated folds with a broad wavelength, and also pop-up structures in the superficial layers. Differently, traces of folds above and below the upper décollement tend to be more parallel if the upper décollement is deeper. Hence, the shallower the upper décollement is, the higher the degree of structural decoupling will become.

Thickness of the upper décollement also played an important role in structural decoupling in our models. It is shown that a thicker upper décollement inhibited the upward growth of folds either through local thinning of the décollement layer on top of anticline hinge zones, or thickening above fold limbs (Fig. 5a). Moreover, a thicker upper décollement provided sufficient materials to fill cores of disharmonic folds formed above the upper décollement during material redistribution (Fig. 5b). Such features are much less distinctive in models with a thinner upper décollement.

4.3. Comparison to the Zagros Fold-and-Thrust Belt

Although the models presented are not aimed for directly simulating structures of any natural prototypes, here it is attempted to compare the modelling results to the Zagros FAT Belt with multidécollements. The Zagros FAT Belt is a NW-SE-trending, 1800 km long segment of the Alpine-Himalayan orogenic belt (Fig. 9a), which has been extensively studied not only because that it is one of the most active collisional belts worldwide (Pirouz et al., 2017), but also due to its specular fold trains developed in a thick multilayer of Paleozoic to Cenozoic sediments that serve as the host to one of the world's largest hydrocarbon provinces (Cooper, 2007). The Early Cambrian Hormuz evaporites serves as the basal décollement for the fold trains to be detached on (Bahroudi and Koyi, 2003). The middle Miocene evaporites of the Gashsaran Formation constitute a relatively shallow upper décollement in the Dezful area (Fig. 9b) (Ghanadian et al., 2017). The Triassic evaporites of the Dashtak Formation is one of the major intermediate décollements in coastal Fars and southwestern Izeh (Fig. 11b) (Najafi et al., 2014). The three major décollements significantly affected the mechanical stratigraphy and rock rheology profile of Zagros (Sepehr et al., 2006) (Fig. 9b).

In the Zagros FAT Belt, most of the shortening of the sedimentary cover has been accommodated by multilayer detachment folding and Hormuz salt diapirism (Motamedi et al., 2011; Najafi et al., 2018). The Gachsaran evaporites have been suggested to have enabled decoupling the surface structures and the deep-seated folds in areas where the evaporites act as the upper décollement (Sherkati et al., 2005; Derikvand et al., 2018; Najafi et al., 2018) (Fig. 9b). Structural decoupling is represented by (1) flow of mobile salt onto underlying synclines; (2) formation of strongly disharmonic, short-wavelength detachment folds above the Gachsaran Formation (Fig. 9c); and (3) termination of some deep-seated thrust faults that encounter the Gachsaran evaporites, and development of minor thrust faults that are originated from the Gachsaran Formation (Ghanadian et al., 2017). Notably, structural decoupling controlled by the Gachsaran evaporites becomes less considerable in the NE sector compared to the SW sector of Deful, due to the decrease in its thickness (Derikvand et al., 2018). The conclusions drawn above largely agree with our modelling results that a shallower and thicker upper décollement contributes to a more profound structural decoupling, especially to the generation of secondary disharmonic folds and thrusts in the shallow strata that do not coincide with the deep-seated structures (Figs 2b, 5b).

The Triassic evaporites of the Dashtak Formation is identified as the main intermediate décollement that effectively shaped the folds in the Fars region (Fig. 9b). The folds developed there mainly include asymmetric faulted box folds. Notably, the fold traces in strata below and above the Dashtak evaporites are approximately parallel, indicating a less degree of structural decoupling than that in the Dezful Embayment. The relatively 'simple' structural styles in the Fars (Blanc et al., 2003) are similar to our modeling results of models 5 and 14 with an intermediate-depth upper décollement. In particular, structural decoupling in the two models is less significant than models with a shallower upper décollement.

It should be noted that the numerical models presented are highly simplified and only show the first order structural similarities to the Zagros FAT Belt. To better reproduce the structures developed in this area, it is suggested that future models should incorporate more comprehensive regional geological data.

5. Conclusions

(1) The models with double décollements and varying parameters produced a range of structural styles as the result of shortening, including sinusoidal detachment folds in models composed of the least competent material, faulted and diapir-cored box folds in models composed of a more competent material, and thrust-dominated piggyback thrust systems and pop-up structures in models composed of the most competent material.

(2) Structural decoupling above and below the upper décollements decreases as rock competence increases. A shallower upper décollement favours the development of minor disharmonic folds and pop-up structures as second-order structures that do not coincide with the deep-seated folds. A thicker upper décollement contributes to the generation of more disharmonic minor folds in the shallow strata by providing sufficient mobile materials to fill fold cores, and remobilization of materials onto synclines, both enhancing structural decoupling.

(3) Our modeling results exhibit first-order structural similarities to the predominant diapir-cored box folds in the Zagros Fold-and-Thrust Belt with multidécollements.

(4) This study demonstrates that rock competence, depth and thickness of the upper décollement can jointly influence thin-skinned tectonics in systems with multiple décollement levels, and determine the degree of structural decoupling.

Acknowledgements

The first author's position is funded by the Sandstone Injection Research Group (SIRG) consortium. Itasca is thanked for technical support. Google Earth™ is acknowledged for providing satellite images.

References

Alsop, G.I., Marco, S., Weinberger, R., Levi, T., 2017. Upslope-verging back thrusts developed during downslope-directed slumping of mass transport deposits. Journal of Structural Geology 100, 45-61.

Bahroudi, A., Koyi, H., 2003. Effect of spatial distribution of Hormuz salt on deformation style in the Zagros fold and thrust belt: an analogue modelling approach. Journal of the Geological Society 160, 719-733.

Benesh, N.P., Plesch, A., Shaw, J.H., Frost, E.K., 2007. Investigation of growth fault bend folding using discrete element modeling: Implications for signatures of active folding above blind thrust faults. Journal of Geophysical Research: Solid Earth 112, B03S04, doi:10.1029/2006JB004466.

Blanc, E.-P., Allen, M.B., Inger, S., Hassani, H., 2003. Structural styles in the Zagros simple folded zone, Iran. Journal of the Geological Society 160, 401-412.

Bonini, M., 2003. Detachment folding, fold amplification, and diapirism in thrust wedge experiments. Tectonics 22, 1065, doi:10.1029/2002TC001458.

Borderie, S., Graveleau, F., Witt, C., Vendeville, B.C., 2018. Impact of an interbedded viscous décollement on the structural and kinematic coupling in fold-and-thrust belts: Insights from analogue modeling. Tectonophysics 722, 118-137.

Burbidge, D.R., Braun, J., 2002. Numerical models of the evolution of accretionary wedges and fold-and-thrust belts using the distinct-element method. Geophysical Journal International 148, 542-561.

Callot, J.-P., Trocmé, V., Letouzey, J., Albouy, E., Jahani, S., Sherkati, S., 2012. Pre-existing salt structures and the folding of the Zagros Mountains. Geological Society, London, Special Publications 363, 545-561.

Chapple, W.M., 1978. Mechanics of thin-skinned fold-and-thrust belts. Geological Society of America Bulletin 89, 1189-1198.

Cooper, M., 2007. Structural style and hydrocarbon prospectivity in fold and thrust belts: a global review. Geological Society, London, Special Publications 272, 447-472.

Cundall, P.A., Strack, O.D.L., 1979. A discrete numerical model for granular assemblies. Geotechnique 29, 47-65.

Cundall, P.A., Strack, O.D.L., 1999. Particle flow code in 2 dimensions. Itasca consulting group, Inc.

Davis, D.M., Engelder, T., 1985. The role of salt in fold-and-thrust belts. Tectonophysics 119, 67-88.

Dean, S.L., Morgan, J.K., Fournier, T., 2013. Geometries of frontal fold and thrust belts: Insights from discrete element simulations. Journal of Structural Geology 53, 43-53.

Derikvand, B., Alavi, S.A., Fard, I.A., Hajialibeigi, H., 2018. Folding style of the Dezful Embayment of Zagros Belt: Signatures of detachment horizons, deep-rooted faulting and syn-deformation deposition. Marine and Petroleum Geology 91, 501-518.

Driehaus, L., Nalpas, T., Ballard, J.-F., 2014. Interaction between deformation and sedimentation in a multidecollement thrust zone: Analogue modelling and application to the Sub-Andean thrust belt of Bolivia. Journal of Structural Geology 65, 59-68.

Erickson, S.G., 1996. Influence of mechanical stratigraphy on folding vs faulting. Journal of Structural Geology 18, 443-450.

Farzipour-Saein, A., Koyi, H., 2016. Intermediate decollement activation in response to the basal friction variation and its effect on folding style in the Zagros fold-thrust belt, an analogue modeling approach. Tectonophysics 687, 56-65.

Feng, L., Bartholomew, M.J., Choi, E., 2015. Spatial arrangement of décollements as a control on the development of thrust faults. Journal of Structural Geology 75, 49-59.

Finch, E., Hardy, S., Gawthorpe, R., 2003. Discrete element modelling of contractional fault-propagation folding above rigid basement fault blocks. Journal of Structural Geology 25, 515-528.

Ghanadian, M., Faghih, A., Fard, I.A., Kusky, T., Maleki, M., 2017b. On the role of incompetent strata in the structural evolution of the Zagros Fold-Thrust Belt, Dezful Embayment, Iran. Marine and Petroleum Geology 81, 320-333.

Hardy, S., Finch, E., 2005. Discrete-element modelling of detachment folding. Basin Research 17, 507-520.

Hardy, S., Finch, E., 2006. Discrete element modelling of the influence of cover strength on basement-involved fault-propagation folding. Tectonophysics 415, 225-238.

Hughes, A.N., Benesh, N.P., Shaw, J.H., 2014. Factors that control the development of fault-bend versus fault-propagation folds: Insights from mechanical models based on the discrete element method (DEM). Journal of Structural Geology 68, 121-141.

Izquierdo-Llavall, E., Roca, E., Xie, H., Pla, O., Muñoz, J.A., Rowan, M.G., Yuan, N., Huang, S., 2018. Influence of Overlapping décollements, Syntectonic Sedimentation, and Structural Inheritance in the Evolution of a Contractional System: The Central Kuqa Fold-and-Thrust Belt (Tian Shan Mountains, NW China). Tectonics 37, 2608-2632.

Liu, Y., Konietzky, H., 2018. Particle-Based Modeling of Pull-Apart Basin Development. Tectonics 37, 343-358.

Massoli, D., Koyi, H.A., Barchi, M.R., 2006. Structural evolution of a fold and thrust belt generated by multiple décollements: analogue models and natural examples from the Northern Apennines (Italy). Journal of Structural Geology 28, 185-199.

McQuarrie, N., 2004. Crustal scale geometry of the Zagros fold–thrust belt, Iran. Journal of Structural Geology 26, 519-535.

Meng, Q., Hodgetts, D., 2019. Combined control of décollement layer thickness and cover rock cohesion on structural styles and evolution of fold belts: A discrete element modelling study. Tectonophysics 757, 58-67.

Morgan, J.K., 2015. Effects of cohesion on the structural and mechanical evolution of fold and thrust belts and contractional wedges: Discrete element simulations. Journal of Geophysical Research: Solid Earth 120, 3870-3896.

Motamedi, H., Sepehr, M., Sherkati, S., Pourkermani, M., 2011. Multi-phase Hormuz salt diapirism in the southern Zagros, SW Iran. Journal of Petroleum Geology 34, 29-43.

Motamedi, H., Sherkati, S., Sepehr, M., 2012. Structural style variation and its impact on hydrocarbon traps in central Fars, southern Zagros folded belt, Iran. Journal of Structural Geology 37, 124-133.

Najafi, M., Vergés, J., Etemad-Saeed, N., Karimnejad, H.R., 2018. Folding, thrusting and diapirism: Competing mechanisms for shaping the structure of the north Dezful Embayment, Zagros, Iran. Basin Research 30, 1200-1229.

Najafi, M., Yassaghi, A., Bahroudi, A., Vergés, J., Sherkati, S., 2014. Impact of the Late Triassic Dashtak intermediate detachment horizon on anticline geometry in the Central Frontal Fars, SE Zagros fold belt, Iran. Marine and Petroleum Geology 54, 23-36.

Naylor, M., Sinclair, H.D., Willett, S., Cowie, P.A., 2005. A discrete element model for orogenesis and accretionary wedge growth. Journal of Geophysical Research: Solid Earth 110, B12403, doi:10.1029/2003JB002940.

Pirouz, M., Avouac, J.-P., Hassanzadeh, J., Kirschvink, J.L., Bahroudi, A., 2017. Early Neogene foreland of the Zagros, implications for the initial closure of the Neo-Tethys and kinematics of crustal shortening. Earth and Planetary Science Letters 477, 168-182.

Ruh, J.B., Kaus, B.J.P., Burg, J.P., 2012. Numerical investigation of deformation mechanics in fold-and-thrust belts: Influence of rheology of single and multiple décollements. Tectonics 31, TC3005,doi:10.1029/2011TC003047.

Schori, M., Mosar, J., Schreurs, G., 2015. Multiple detachments during thin-skinned deformation of the Swiss Central Jura: a kinematic model across the Chasseral. Swiss Journal of Geosciences 108, 327-343.

Sepehr, M., Cosgrove, J., Moieni, M., 2006. The impact of cover rock rheology on the style of folding in the Zagros fold-thrust belt. Tectonophysics 427, 265-281.

Sherkati, S., Letouzey, J., Frizon de Lamotte, D., 2006. Central Zagros fold-thrust belt (Iran): New insights from seismic data, field observation, and sandbox modeling. Tectonics 25, TC4007, doi:10.1029/2004TC001766.

Sherkati, S., Molinaro, M., de Lamotte, D.F., Letouzey, J., 2005. Detachment folding in the Central and Eastern Zagros fold-belt (Iran): salt mobility, multiple detachments and late basement control. Journal of Structural Geology 27, 1680-1696.

Stewart, S.A., 1996. Influence of detachment layer thickness on style of thin-skinned shortening. Journal of Structural Geology 18, 1271-1274.

Stewart, S. A., 1999. Geometry of thin-skinned tectonic systems in relation to detachment layer thickness in sedimentary basins. Tectonics 18, 719-732.

Table 1. Summary of modelling results of the discrete element models.

Model series	Number	Relative depth of the upper décollement	Relative thickness of the upper décollement	Number of diapirs	Max. diapir height (km)	Surface uplift (km)		Length of undeformed foreland (km)	Structural styles	Distinct structural decoupling, Y/N
						Min.	Max.			
S1	1	shallow	thinner	8	0.48	1.13	1.63	0	sinusoidal folds, box folds,	Y
	2	shallow	thinner	4	1.13	0	1.79	2.20	box fold	Y
	3	shallow	thinner	3	1.36	0	3.10	5.67	piggyback thrusts	Y
S2	4	intermediate	thinner	8	0.37	0.30	1.87	0	sinusoidal folds, box folds,	Y
	5	intermediate	thinner	4	1.49	0	1.85	2.33	box folds, fault-propagation folds	N
	6	intermediate	thinner	4	1.89	0	2.75	5.26	piggyback thrusts, fault-bend folds	N
S3	7	deep	thinner	11	0.42	0.29	1.82	0	sinusoidal folds	Y
	8	deep	thinner	3	1.59	0	1.72	4.46	box fold, fault-propagation fold	N
	9	deep	thinner	1	2.94	0	2.49	6.04	fault-bend fold, tensile fractures	N
S4	10	shallow	equal	7	0.51	0.27	1.84	0	box folds, sinusoidal folds	Y
	11	shallow	equal	6	1.09	0	1.93	1.87	box folds	Y
	12	shallow	equal	2	1.66	0	4.68	5.37	piggyback thrusts, fault-propagation fold	Y
S5	13	intermediate	equal	8	0.35	0.27	1.85	0	sinusoidal folds, box folds	Y
	14	intermediate	equal	4	1.44	0	1.95	2.24	box folds	N
	15	intermediate	equal	2	2.11	0	3.15	5.41	fault-propagation and bend folds, tensile fractures	N
S6	16	deep	equal	5	0.37	0.24	2.11	0	sinusoidal folds, box folds	Y
	17	deep	equal	3	1.56	0	1.99	1.13	box folds, fault-propagation folds	N
	18	deep	equal	2	1.93	0	2.91	5.16	fault-propagation and bend folds, tensile fractures	N

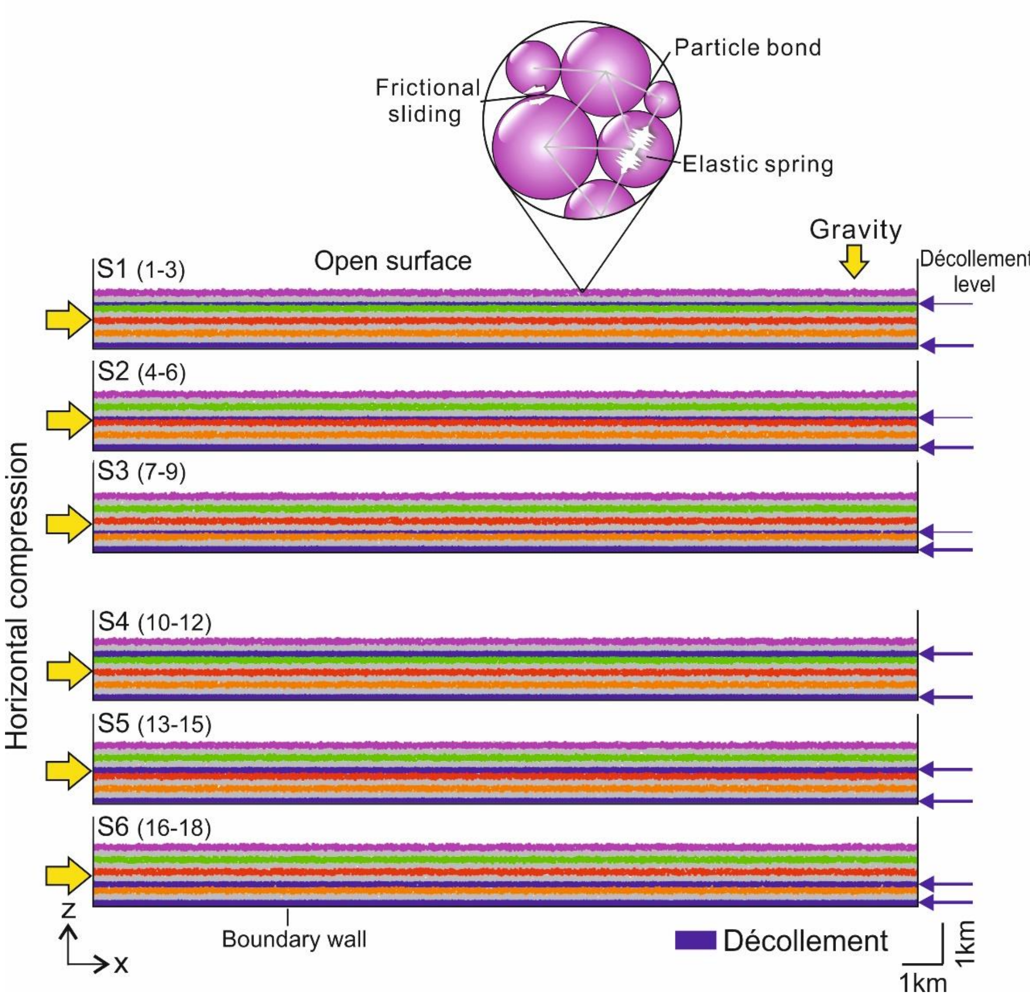

Fig. 1. (a) Design and boundary conditions of the discrete element models. Models of series 1-3 contain a thinner upper décollement than the basal décollement. Models of series 4-6 contain two equally thick décollements. The enlarged circular area shows particle interactions.

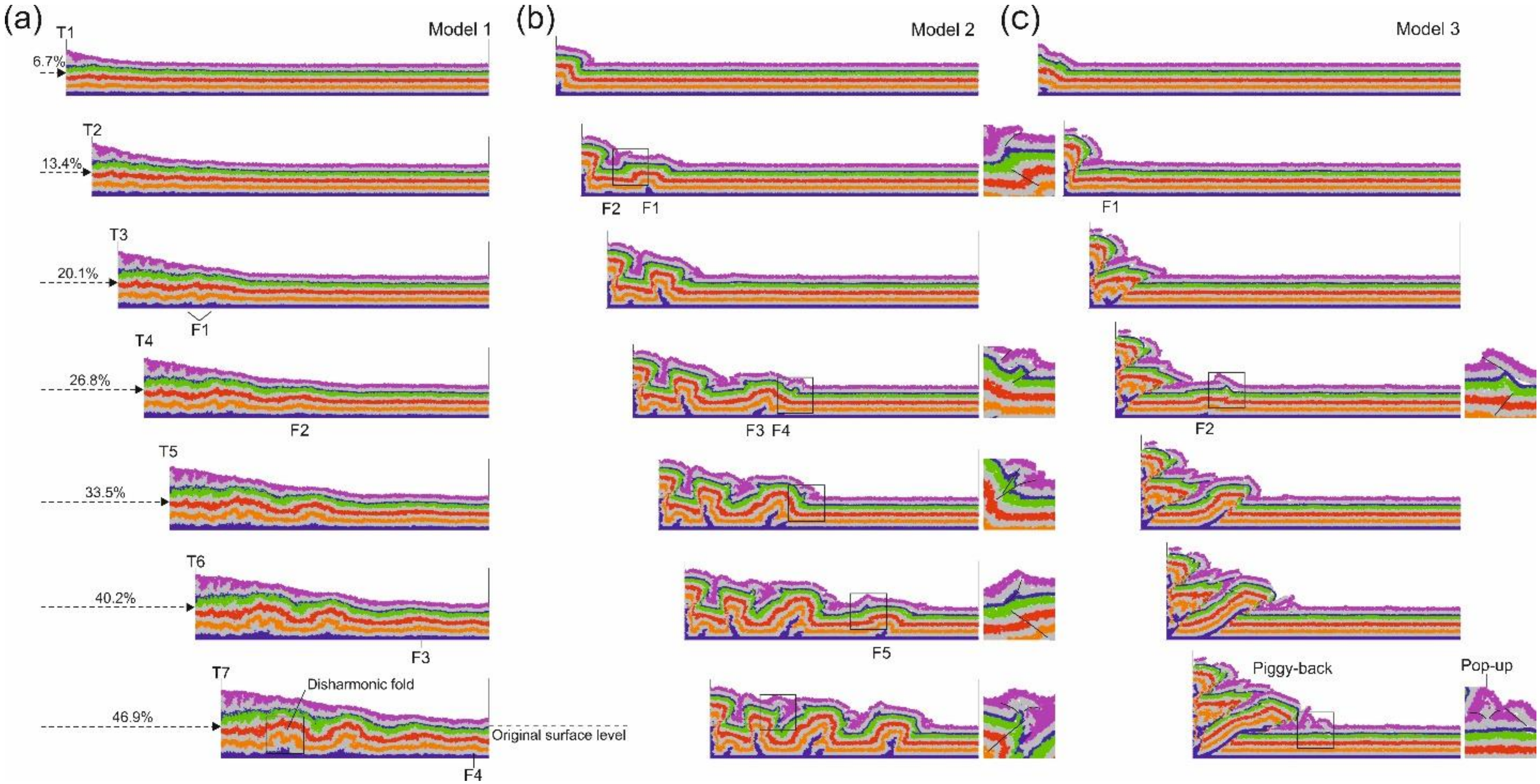

Fig. 2. Modelling results of model 1 (a), model 2 (b) and model 3 (c) in series 1. The enlarged boxes show features of structural decoupling above and below the upper décollement.

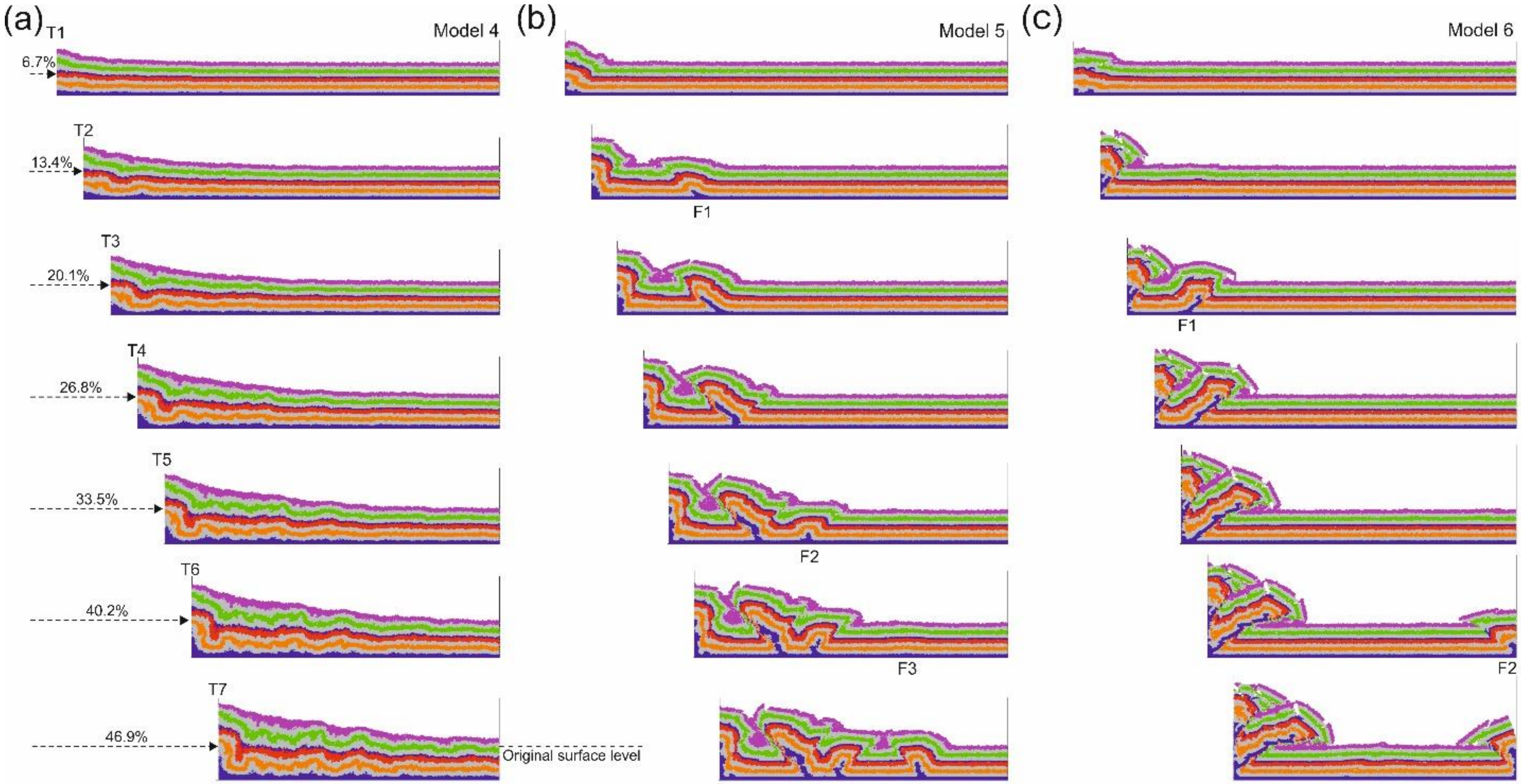

Fig. 3. Modelling results of model 4 (a), model 5 (b) and model 6 (c) in series 2.

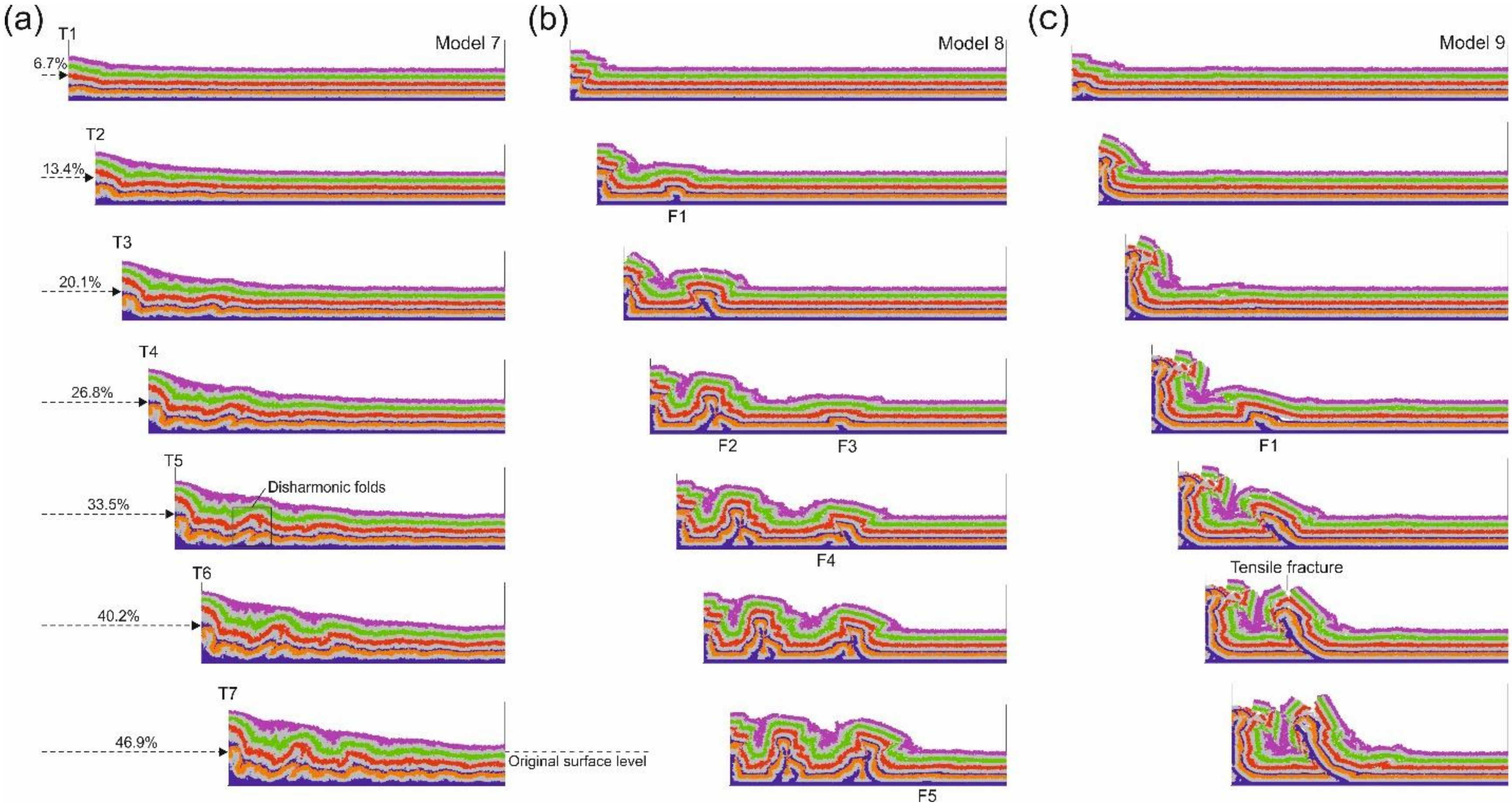

Fig. 4. Modelling results of model 7 (a), model 8 (b) and model 9 (c) in series 3.

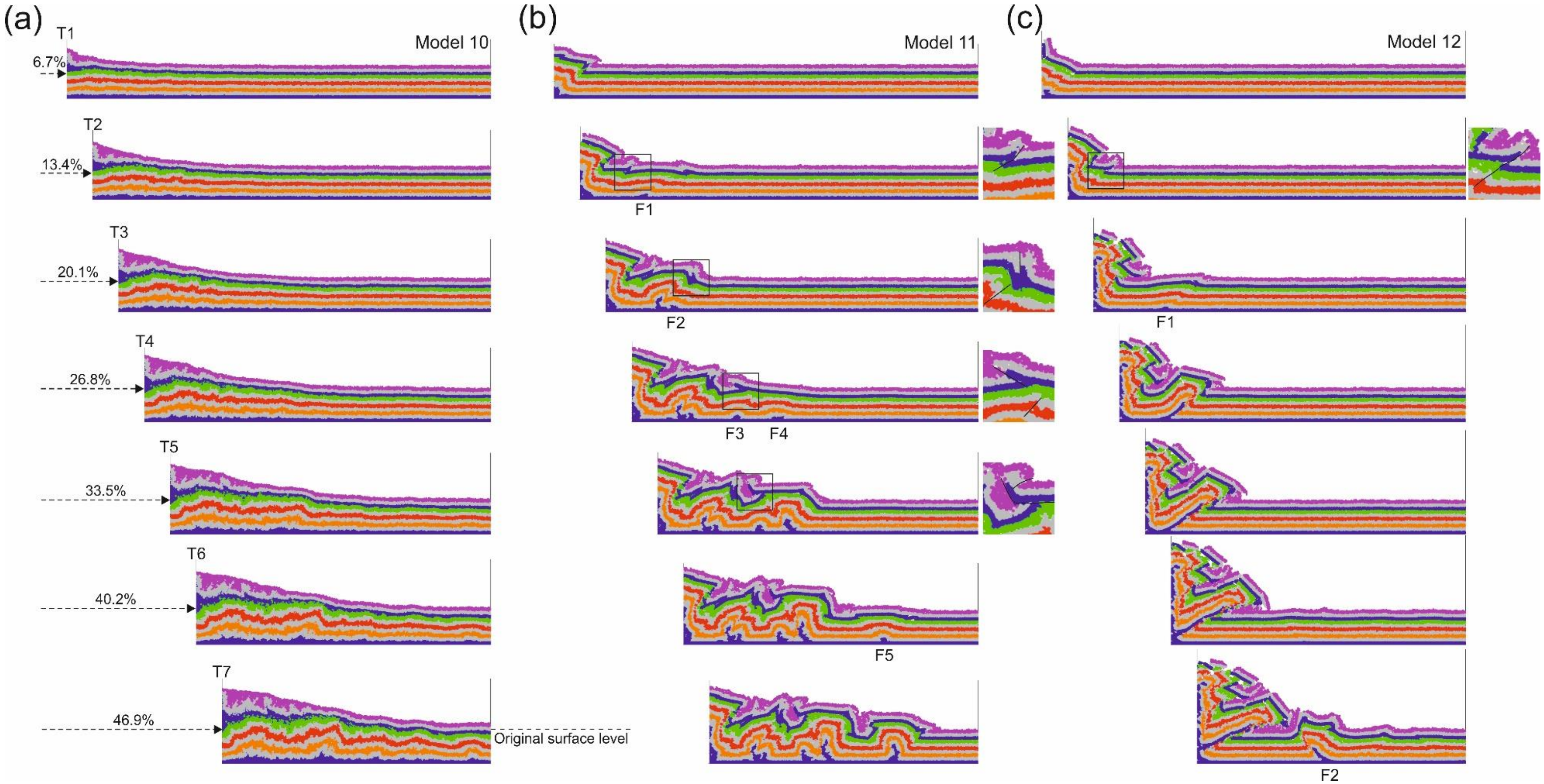

Fig. 5. Modelling results of model 10 (a), model 11 (b) and model 12 (c) in series 4. The enlarged boxes show features of structural decoupling above and below the upper décollement.

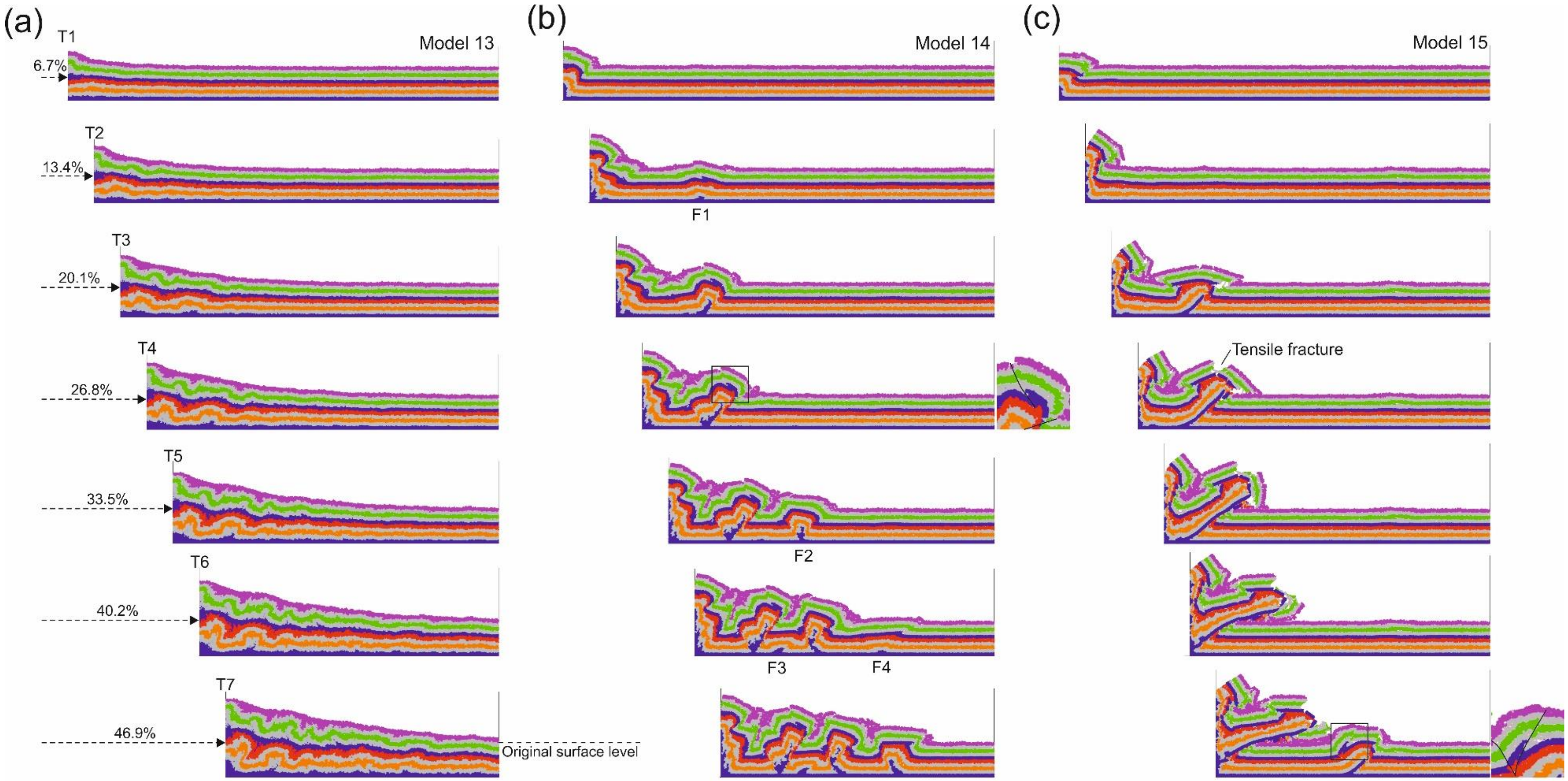

Fig. 6. Modelling results of model 13 (a), model 14 (b) and model 15 (c) in series 5. The enlarged boxes show features of structural decoupling above and below the upper décollement.

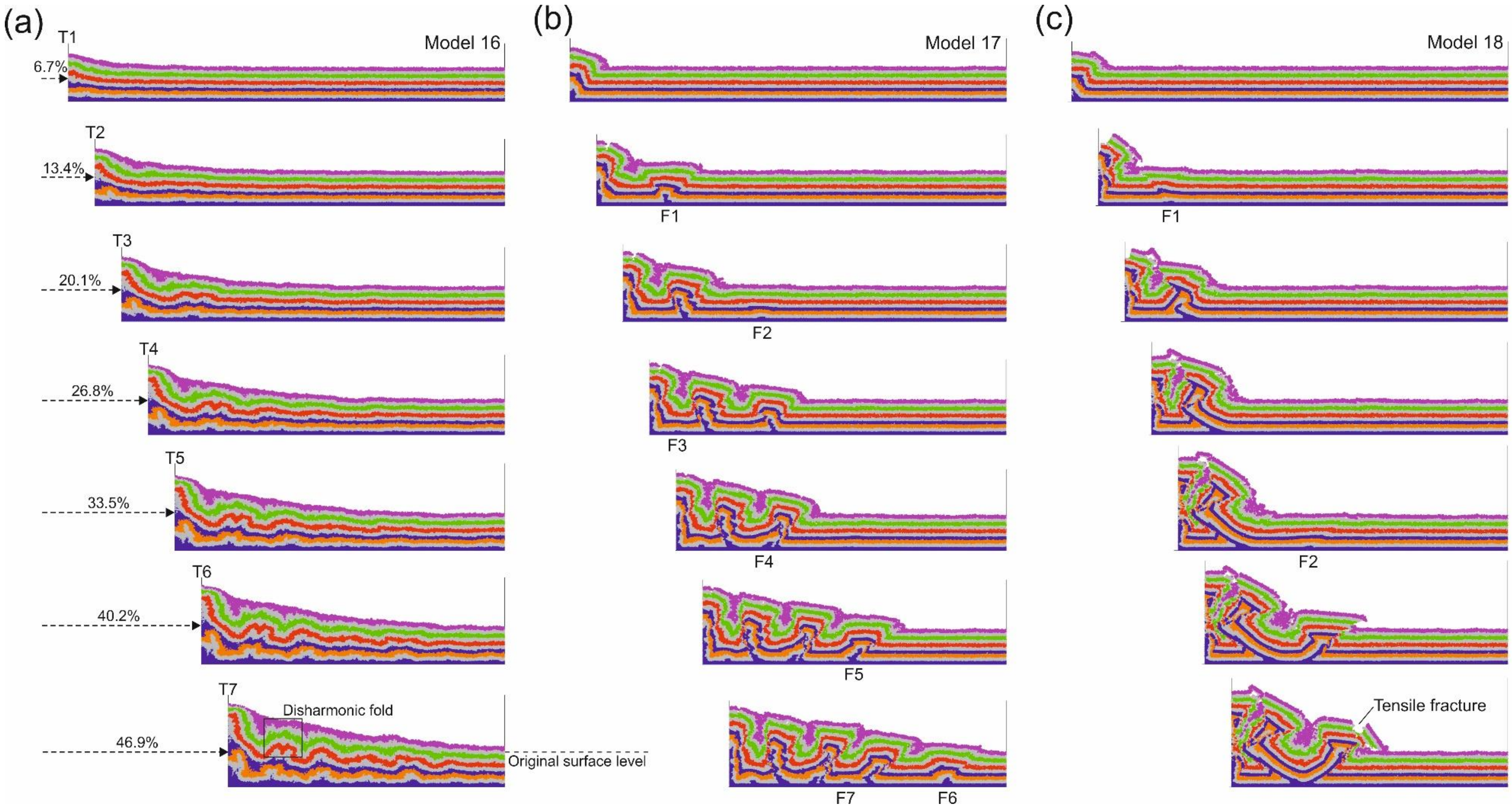

Fig. 7. Modelling results of model 16 (a), model 17 (b) and model 18 (c) in series 6.

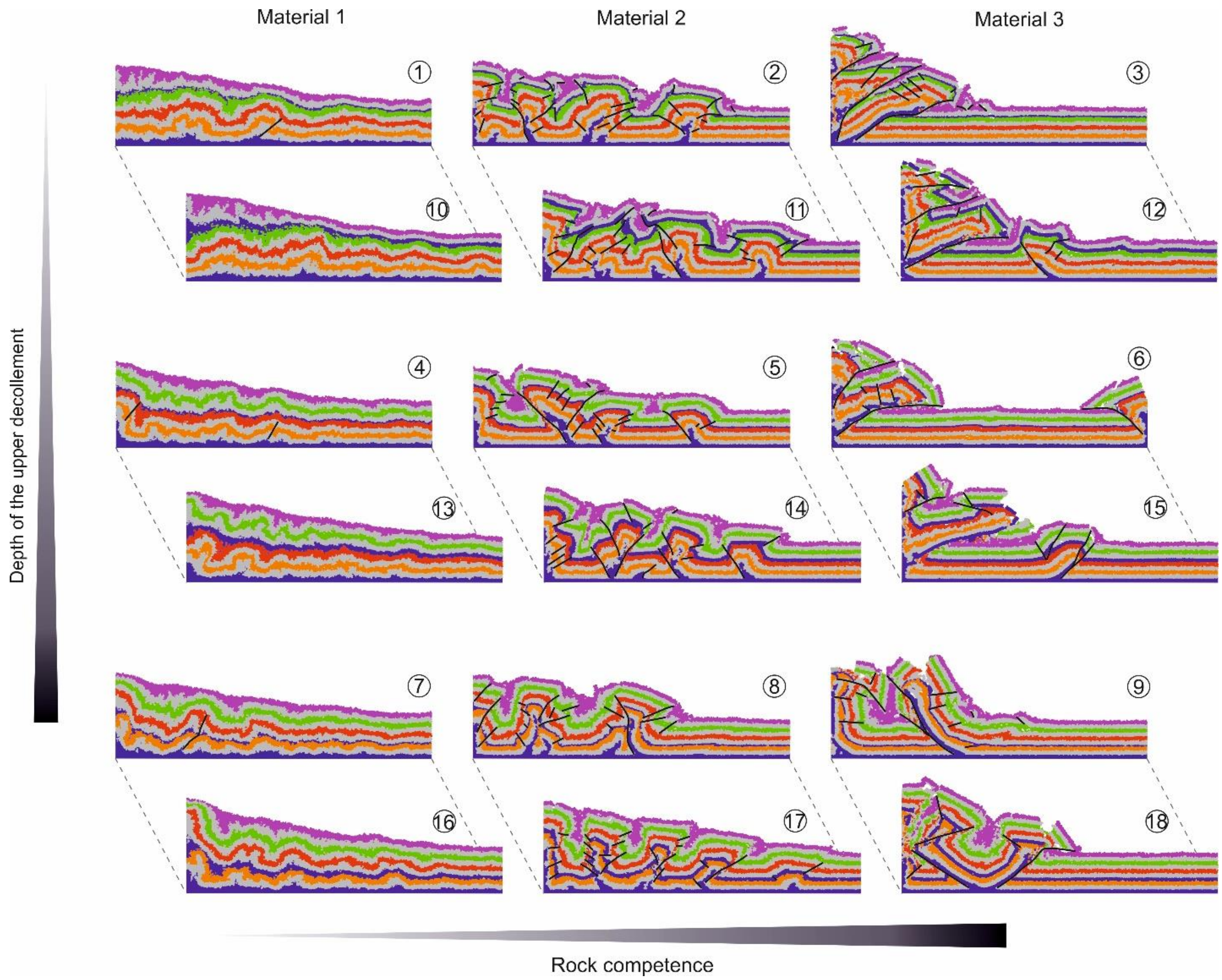

Fig. 8. Summary of modelling results of all models. Fault traces are highlighted by black solid lines.

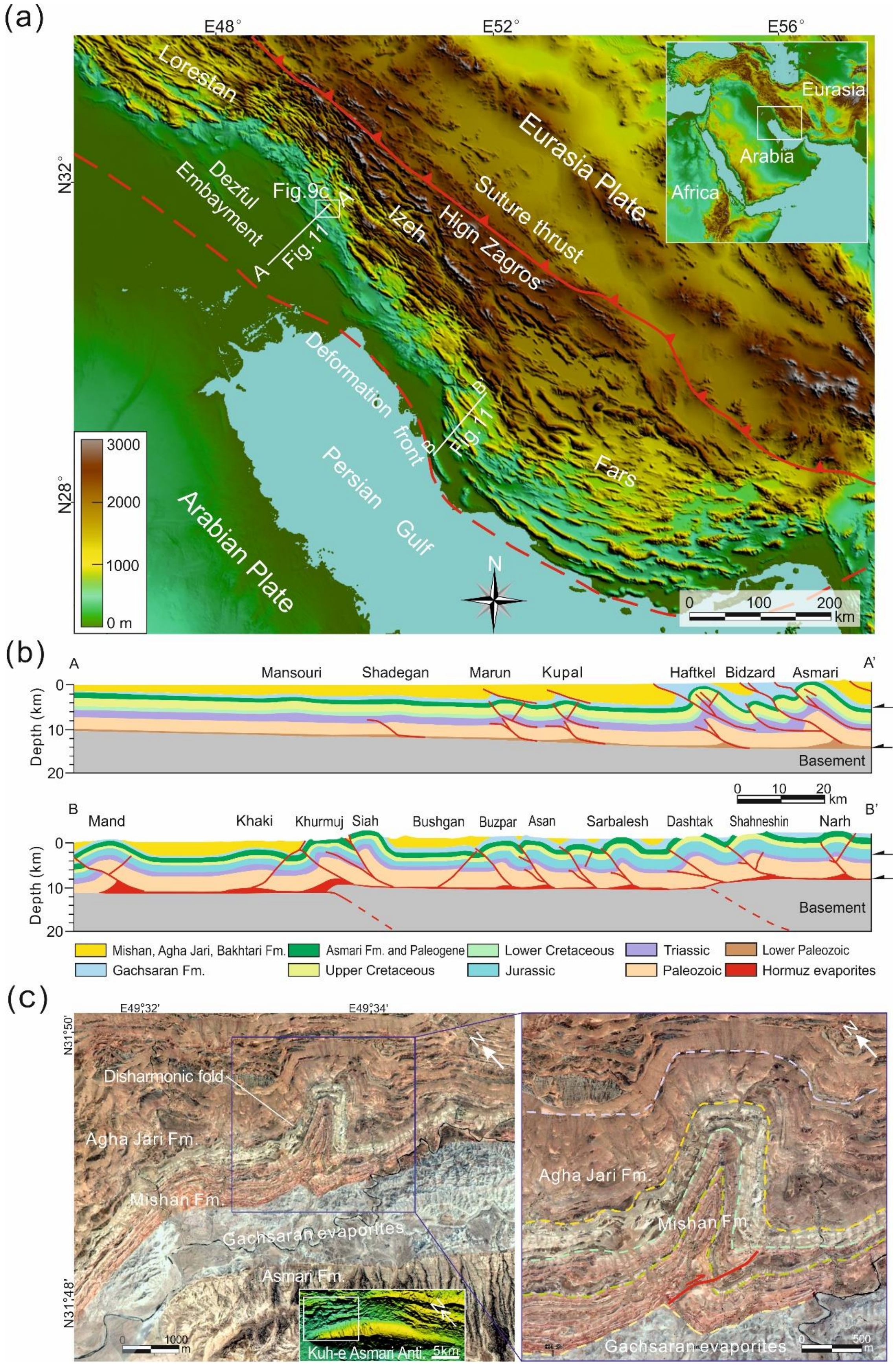
(a)
E48°
E52°
E56°
N32°
N28°
Lorestan
Dezful Embayment
Fig.9c
Fig.11
A
A'
Izeh
High Zagros
Suture thrust
Eurasia Plate
Eurasia
Arabia
Africa
Deformation front
Persian Gulf
Fig.11
B
B'
Fars
Arabian Plate
3000
2000
1000
0 m
N
0 100 200 km
(b)
A
A'
Mansouri
Shadegan
Marun
Kupal
Haftkel
Bidzard
Asmari
Depth (km)
0
10
20
Basement
0 10 20 km
B
B'
Mand
Khaki
Khurmuj
Siah
Bushgan
Buzpar
Asan
Sarbalesh
Dashtak
Shahneshin
Narh
Mishan, Agha Jari, Bakhtari Fm.
Asmari Fm. and Paleogene
Lower Cretaceous
Triassic
Lower Paleozoic
Gachsaran Fm.
Upper Cretaceous
Jurassic
Paleozoic
Hormuz evaporites
(c)
E49°32'
E49°34'
N31°50'
N31°48'
Disharmonic fold
Agha Jari Fm.
Mishan Fm.
Gachsaran evaporites
Asmari Fm.
0 1000 m
Kuh-e Asmari Anti.
5km
N
Agha Jari Fm.
Mishan Fm.
Gachsaran evaporites
0 500 m

Fig. 9. (a) Elevation map showing the location and main structural elements of the Zagros Fold-and-Thrust Belt. (b) Cross sections of the Dezful Embayment and the Fars province. Modified from Sherkati et al (2006). See locations in Fig. 9a. (c) Google satellite image showing outcrop exposure of a minor disharmonic fold developed above the shallow Gachsaran evaporites in the Kuh-e Asmari Anticline. The image is located in the box area of the elevation map that shows the fold geometry. The enlarged box shows details of the disharmonic fold. The dashed lines highlight the bedding traces as markers for correlation. The reverse fault is marked by the red line. See location in Fig. 9a.